Pulsar Wind Nebulae

Patrick Slane

Abstract The extended nebulae formed as pulsar winds expand into their surroundings provide information about the composition of the winds, the injection history from the host pulsar, and the material into which the nebulae are expanding. Observations from across the electromagnetic spectrum provide constraints on the evolution of the nebulae, the density and composition of the surrounding ejecta, the geometry of the central engines, and the long-term fate of the energetic particles produced in these systems. Such observations reveal the presence of jets and wind termination shocks, time-varying compact emission structures, shocked supernova ejecta, and newly formed dust. Here I provide a broad overview of the structure of pulsar wind nebulae, with specific examples from observations extending from the radio band to very high energy gamma-rays that demonstrate our ability to constrain the history and ultimate fate of the energy released in the spin-down of young pulsars.

1 Introduction

The explosion of a supernova triggered by the collapse of a massive star produces several solar masses of stellar ejecta expanding at $\sim 10^4$ km s^{-1} into surrounding circumstellar (CSM) and interstellar (ISM) material. The resulting forward shock compresses and heats the ambient gas. As the shock sweeps up material, the deceleration drives a reverse shock (RS) back into the cold ejecta, heating the metal-enhanced gas to X-ray-emitting temperatures. In many cases, though the actual fraction remains a currently-unsolved question, what remains of the collapsed core is a rapidly-spinning, highly magnetic neutron star that generates an energetic wind of particles and magnetic field confined by the surrounding ejecta. [All current evidence indicates that pulsar winds are composed of electrons and positrons, with little

Patrick Slane

Harvard-Smithsonian Center for Astrophysics, e-mail: `slane@cfa.harvard.edu`

or no ion component. Here, and throughout, the term "particles" is used interchangeably for electrons/positrons.] The evolution of this pulsar wind nebula (PWN) is determined by the properties of the central pulsar, its host supernova remnant (SNR), and the structure of the surrounding CSM/ISM.

In discussing the structure and evolution of PWNe, it is important to distinguish two important points at the outset. First, while PWNe have, in the past, sometimes been referred to as SNRs (most often as a "center-filled" variety), they are, in fact, *not* SNRs. As discussed below, PWNe are created entirely by a confined magnetic wind produced by an energetic pulsar. At early times, the confining material is supernova ejecta, but at later times it can simply be the ISM. Despite being the result of a supernova explosion (as is a neutron star), we reserve the term SNR for the structure produced by the expanding supernova ejecta and its interaction with the surrounding CSM/ISM (and, indeed, an entire population of SNRs have no association with PWNe whatsoever; see Chapter "Type Ia supernovae"). Second, when describing the evolutionary phase of a PWN (or a composite SNR – an SNR that contains a PWN), it is not necessarily the true age of the system that describes its structure. Rather, it is the *dynamical* age, which accounts for the fact that identical pulsars expanding into very different density distributions, for example, will evolve differently.

The outline of this paper is as follows. In Section 2 we review the basic properties of pulsars themselves, including a description of pulsar magnetospheres and the subsequent pulsar winds that form PWNe. Section 3 discusses the emission from PWNe and provides examples of the constraints that multiwavelength observations place on the determination of the system evolution. In Section 4 we investigate the different stages of evolution for a PWN, starting with its initial expansion inside an SNR and ending with the bow shock stage after the PWN escapes into the ISM. Section 5 presents a brief summary. Crucially, in the spirit of this Handbook, this paper is not intended as a literature review. A small set of examples have been selected to illustrate particular properties, and a subset of the recent theoretical literature has been summarized to provide the framework for our basic understanding of these systems. The reader is referred to more thorough PWN reviews by Gaensler & Slane (2006), Bucciantini (2011), and Kargaltsev et al. (2015), and to the many references and subsequent citations in those works, for a more detailed treatment.

2 Basic Properties

2.1 Pulsars

The discovery and basic theory of pulsars has been summarized in many places. First discovered by their radio pulsations, it was quickly hypothesized that these objects are rapidly-rotating, highly-magnetic neutron stars (NSs). Observations show that the spin period P of a given pulsar increases with time, indicating a gradual decrease

in rotational kinetic energy:

$$\dot{E} = I\Omega\dot{\Omega}, \tag{1}$$

where $\Omega = 2\pi/P$ and I is the moment of inertia of the NS (nominally $I = \frac{2}{5}MR^2$, where M and R are the mass and radius of the star; $I \approx 10^{45}$ g cm^2 for $M = 1.4\, M_\odot$ and $R = 10$ km). This spin-down energy loss is understood to be the result of a magnetized particle wind produced by the rotating magnetic star. Treated as a simple rotating magnetic dipole, the energy loss rate is

$$\dot{E} = -\frac{B_p R^6 \Omega^4}{6c^3} \sin^2 \chi, \tag{2}$$

where B_p is the magnetic dipole strength at the pole and χ is the angle between the magnetic field and the pulsar rotation axis. Typical values for P range from $\sim 0.03 - 3$s, with period derivatives of $10^{-17} - 10^{-13}$ s s^{-1} (though values outside these ranges are also observed, particularly for so-called magnetars and millisecond pulsars). This leads to inferred magnetic field strengths of order $10^{11} - 10^{13}$ G.

As the pulsar rotates, a charge-filled magnetosphere is created, with particle acceleration occurring in charge-separated gaps in regions near the polar cap or in the outer magnetosphere, which extends to the so-called light cylinder where $R_{\mathrm{LC}} = c/\Omega$. The maximum potential generated by the rotating pulsar field under the assumption of co-alignment of the magnetic and spin axes is

$$\Phi = \left(\frac{\dot{E}}{c}\right) \approx 6 \times 10^{13} \left(\frac{\dot{E}}{10^{38} \text{ erg s}^{-1}}\right)^{1/2} \text{ V}. \tag{3}$$

The minimum particle current required to sustain the charge density in the magnetosphere is

$$\dot{N}_{GJ} = \frac{c\Phi}{e} \approx 4 \times 10^{33} \left(\frac{\dot{E}}{10^{38} \text{ erg s}^{-1}}\right)^{1/2} \text{ s}^{-1}, \tag{4}$$

where e is the electron charge (Goldreich & Julian 1969). As the particles comprising this current are accelerated, they produce curvature radiation that initiates an electron-positron pair cascade. Based on observations of PWNe, values approaching $\dot{N} = 10^{40}$ s^{-1} are required to explain the radio synchrotron emission. The implied multiplicity (i.e., the number of pairs created per primary particle) of $\sim 10^5 - 10^7$ appears difficult to obtain from pair production in the acceleration regions within pulsar magnetospheres (Timokhin & Harding 2015), suggesting that a relic population of low energy electrons created by some other mechanism early in the formation of the PWN may be required (e.g., Atoyan & Aharonian 1996).
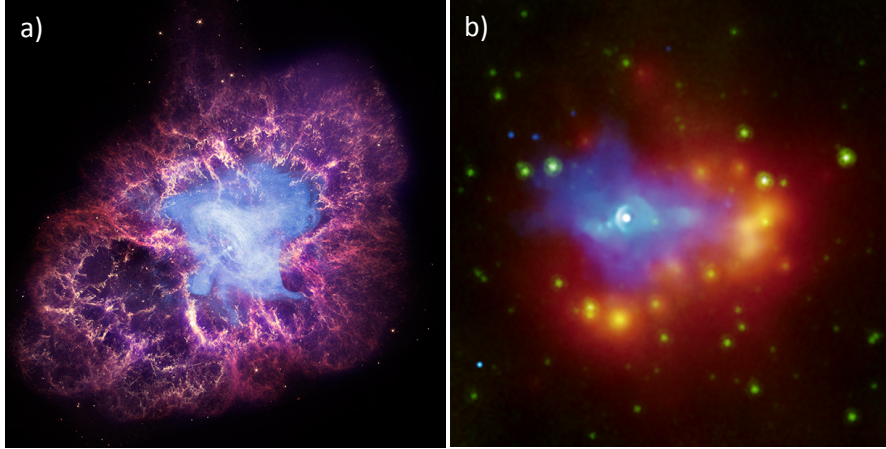
Fig. 1 a) Composite image of Crab Nebula with X-ray emission (blue) from *Chandra*, optical emission (red and yellow) from *HST*, and IR emission (purple) from *Spitzer*. b) Composite image of G54.1+0.3 (Temim et al. 2010) with X-ray emisson (blue) from *Chandra*, and IR emission from *Spitzer* (red-yellow, 24μm; green, 8μm). [Images courtesy NASA/CXO.]

2.2 Pulsar Wind Nebulae

For pulsars with a magnetic axis that is inclined relative to the rotation axis, the result of the above is a striped wind, with an alternating poloidal magnetic field component separated by a current sheet (Bogovalov 1999). The magnetization of the wind, σ, is defined as the ratio between the the Poynting flux and the particle energy flux:

$$\sigma = \frac{B^2}{4\pi mn\gamma_0 c^2},$$ (5)

where B, n, and γ_0 are the magnetic field, number density of particles of mass m, and bulk Lorentz factor in the wind, respectively. The energy density of the wind is expected to be dominated by the Poynting flux as it leaves the magnetosphere, with $\sigma \sim 10^4$. Ultimately, the wind is confined by ambient material (slow-moving ejecta in the host SNR at early times; the ISM once the pulsar has exited the SNR), forming an expanding magnetic bubble of relativistic particles - the PWN. As the fast wind entering the nebula decelerates to meet the boundary condition imposed by the much slower expansion of the PWN, a wind termination shock (TS) is formed at a radius R_{TS} where the ram pressure of the wind is balanced by the pressure within the nebula:

$$R_{\text{TS}} = \sqrt{\dot{E}/(4\pi\omega c P_{\text{PWN}})},$$ (6)

where ω is the equivalent filling factor for an isotropic wind and P_{PWN} is the total pressure in the nebula. The geometry of the pulsar system results in an axisymmetric wind (Lyubarsky 2002), forming a torus-like structure in the equatorial plane, along

with collimated jets along the rotation axis. The higher magnetization at low latitudes confines the expansion here to a higher degree, resulting in an elongated shape along the pulsar spin axis for the large-scale nebula (Begelman & Li 1992, van der Swaluw 2003). This structure is evident in Figure 1 (left), where X-ray and optical observations of the Crab Nebula clearly reveal the jet/torus structure surrounded by the elongated wind nebula bounded by filaments of swept-up ejecta. The innermost ring corresponds to the TS, and its radius is well-described by Eqn. 6. MHD models of the jet/torus structure in pulsar winds reproduce many of the observed details of these systems (see Bucciantini 2011 for a review).

As discussed in Section 3, the relativistic particles in the PWN produce synchrotron radiation extending from the radio to the X-ray band, and upscatter ambient low-energy photons (from the cosmic microwave background, the stellar radiation field, and emission from ambient dust) producing inverse-Compton (IC) emission in the γ-ray band. Curiously, models of the dynamical structure and emission properties of the Crab Nebula require $\sigma \sim 10^{-3}$ just upstream of the termination shock (Kennel & Coroniti 1984). Thus, somewhere between the pulsar magnetosphere and the termination shock, the wind converts from being Poynting-dominated to being particle-dominated. Magnetic reconnection in the current sheet has been suggested as a mechanism for dissipating the magnetic field, transferring its energy into that of the particles (e.g., Lyubarsky 2003). Recent particle-in-cell simulations of relativistic shocks show that shock compression of the wind flow can drive regions of opposing magnetic fields together, causing the reconnection (Sironi & Spitkovsky 2011). As discussed in Section 3, this process can result in a broad particle spectrum, with a power-law-like shape $dN/dE \propto E^{-p}$ with $p \sim 1.5$. High energy particles in the equatorial regions can diffuse upstream of the shock, generating turbulence that supports acceleration of subsequent particles to high energies through a Fermi-like process, potentially creating a steeper high-energy tail with $p \sim 2.5$. The energy range spanned by the flat spectral region, and the maximum energy to which the steep spectrum extends, depend on properties of the striped wind that change with latitude, suggesting that the integrated particle injection spectrum may be quite complex (e.g., Slane et al. 2008). However, the maximum Lorentz factor that appears achievable is limited by the requirement that the diffusion length of the particles be smaller than termination shock radius; $\gamma_{max} \sim 8.3 \times 10^6 \dot{E}_{38}^{3/4} \dot{N}_{40}^{-1/2}$. This is insufficient to explain the observed X-ray synchrotron emission in PWNe, suggesting that an alternative picture for acceleration of the highest energy particles in PWNe is required (Sironi et al. 2013).

3 Radiation from PWNe

The emission from PWNe can be divided into two broad categories – that originating from the relativistic particles within the nebula and that produced by material that has been swept up by the nebula.
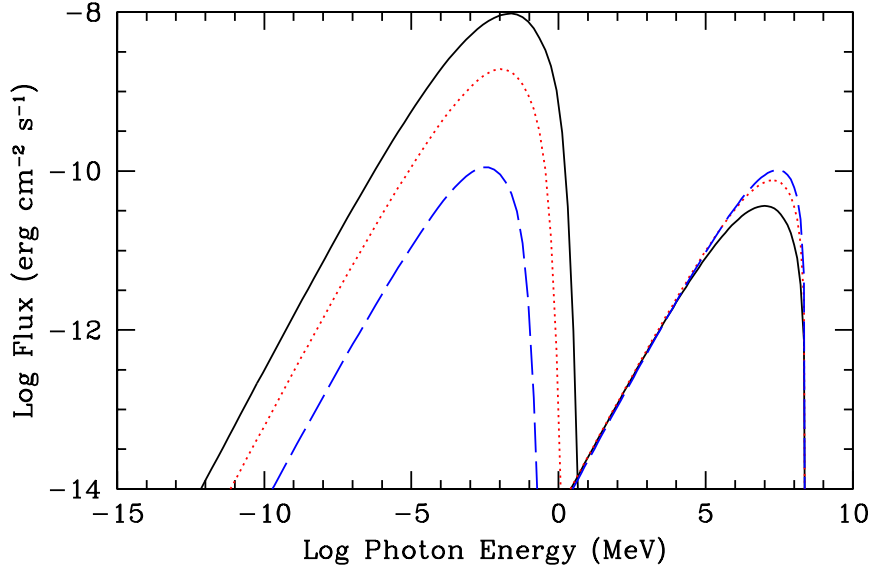
Fig. 2 Synchrotron (left) and IC (right) emission (for scattering off of the CMB) from a PWN at ages of 1000 (solid), 2000 (dotted), and 5000 (dashed) years. Here we have assumed $E_{51} = 1$, $M_{ej} = 8M_\odot$, and $n_0 = 0.1$ cm^{-3} for the SNR evolution, and $n = 3$, $\dot{E}_0 = 10^{40}$ erg s^{-1}, and $\tau_0 = 500$ yr for the pulsar. For the wind, we assume that 99.9% of the energy is in the form of electrons/positrons with a power law spectrum with $\gamma = 1.6$.

3.1 Emission from nebula

The emission from the relativistic particles is a combination of synchrotron radiation and IC radiation associated with the upscattering of ambient photons. If we characterize the injected spectrum as a power law,

$$Q(E_e, t) = Q_0(t)(E_e/E_0)^{-\gamma} \tag{7}$$

the integrated particle energy is then

$$\int Q(E, t)E dE = (1 + \sigma)\dot{E}(t) \tag{8}$$

The resulting emission spectrum is found by integrating the electron spectrum over the emissivity function for synchrotron and IC radiation using, respectively, the nebular magnetic field and spectral density of the ambient photon field. As noted above, the low energy particles in PWNe actually appear to have a flatter spectrum, leading to a flat radio spectrum ($\alpha \sim 0.0 - 0.3$ where $S_\nu \propto \nu^{-\alpha}$) [Note: In X-rays, it is conventional to express the photon spectrum $dN_\gamma/dE \propto E^{-\Gamma}$, where $\Gamma = \alpha + 1$.] The spectrum generally steepens near the mm or optical band. For young PWNe with very high magnetic fields, up-scattering of the high energy synchrotron spectrum

can produce γ-ray photons through so-called synchrotron self-Compton emission. The resulting spectrum thus depends on the age, magnetic field, and pulsar spin-down power (e.g., Torres et al. 2013).

As illustrated in Figure 2, the build-up of particles in the nebula results in an IC spectrum that increases with time. The synchrotron flux decreases with time due to the steadily decreasing magnetic field strength associated with the adiabatic expansion of the PWN (see Section 4). This behavior is reversed upon arrival of the SNR RS (not shown in Figure 2), following which the nebula is compressed and the magnetic field strength increases dramatically, inducing an episode of rapid synchrotron losses. Upon re-expanding, however, IC emission again begins to increase relative to the synchrotron emission. At the latest phases of evolution, when the nebula is very large and the magnetic field is low, the IC emission can provide the most easily-detected signature. As described below, such behavior is seen for a number of PWNe that have been identified based on their emission at TeV energies, and for which only faint synchrotron emission near the associated pulsars is seen in the X-ray band.

For electrons with energy $E_{e,100}$, in units of 100 TeV, the typical energy of synchrotron photons is

$$E_\gamma^s \approx 2.2 E_{e,100}^2 B_{10} \text{ keV}, \tag{9}$$

where B_{10} is the magnetic field strength in units of 10 μG. The associated synchrotron lifetime for the particles is

$$\tau_{syn} \approx 820 E_{e,100}^{-1} B_{10}^{-2} \text{ yr} \tag{10}$$

which results in a break in the photon spectrum at

$$E_{\gamma,br} \approx 1.4 B_{10}^{-3} t_{\text{kyr}}^{-2} \text{ keV} \tag{11}$$

for electrons injected over a lifetime t_{kyr}. Beyond this energy, the photon power law spectrum steepens by $\Delta\Gamma = 0.5$. For young PWNe, with large magnetic fields, the result is a steepening of the X-ray spectrum with radius due to synchrotron burn-off of the higher energy particles on timescales shorter than their transit time to the outer portions of the PWN. This is readily observed in young systems such as G21.5$-$0.9 and 3C 58 (see below), although the spectral index actually flattens more slowly than expected unless rapid particle diffusion is in effect (Tang & Chevalier 2012).

For γ-rays produced by IC-scattering off of the CMB,

$$E_\gamma^{IC} \approx 0.32 E_{e,10}^2 \text{ TeV}, \tag{12}$$

where $E_{e,10} = E_e/(10 \text{ TeV})$. Note that while the synchrotron energy depends upon both the electron energy and the magnetic field strength, the IC energy (from CMB scattering) depends only on the particle energy. Modeling of both emission components for a particular PWN thus allows determination of the magnetic field strength.

Because of the short synchrotron lifetime for the X-ray emitting particles, the X-ray luminosity is related to the current spin-down power of the pulsar. From a

variety of studies, $L_x \sim 10^{-3}\dot{E}$ (e.g., Possenti et al. 2002). Although flux values for individual pulsars may differ from this relationship by as much as a factor of 10, determination of the X-ray luminosity can provide a modest constraint on $\dot{E}$ for systems in which pulsations are not directly detected.

The broadband spectrum of a PWN, along with the associated dynamical information provided by measurements of the pulsar spin properties, and the size of the PWN and its SNR, place very strong constraints on its evolution and on the spectrum of the particles injected from the pulsar. Combined with estimates of the swept-up ejecta mass, this information can be used to probe the properties of the progenitor star and to predict the long-term fate of the energetic particles in the nebula. Recent multiwavelength studies of PWNe, combined with modeling efforts of their evolution and spectra, have provided unique insights into several of these areas.

3.2 Emission from shocked ejecta

As the PWN expands into the surrounding supernova ejecta, as described below, it heats the ejecta. The resulting emission, often confined to filaments, is a combination of radiation from shocked gas and continuum emission from dust condensed from the cold ejecta in the early adiabatic expansion of the SNR. The thermal emission depends on the velocity of the PWN shock driven into the ejecta which, in turn, depends on the spin-down power of the central pulsar and the density and velocity profile of the ejecta. For slow shocks, line emission may be observed in the IR and optical bands, such as that observed from the Crab Nebula (see Chapter "Supernova of 1054 and its remnant, the Crab Nebula"), G21.5−0.9, and G54.1+0.3 (see below), while for faster shocks the emission may appear in the X-ray band, as observed in 3C 58. This line emission can provide important information on the ejecta composition and expansion velocity.

The dust emission is in the form of a blackbody-like spectrum whose properties depend on the temperature, composition, and grain-size distribution of the dust. Measurements of emission from ejecta dust prior to interaction with the SNR RS (see below) are of particular importance in estimating dust formation rates in supernovae (e.g., Temim et al. 2015)

4 PWN Evolution

The evolution of a PWN within the confines of its host SNR is determined by both the rate at which energy is injected by the pulsar and by the density structure of the ejecta material into which the nebula expands. The location of the pulsar itself, relative to the SNR center, depends upon any motion given to the pulsar in the form of a kick velocity during the explosion, as well as on the density distribution of the ambient medium into which the SNR expands. At the earliest times, the SNR blast
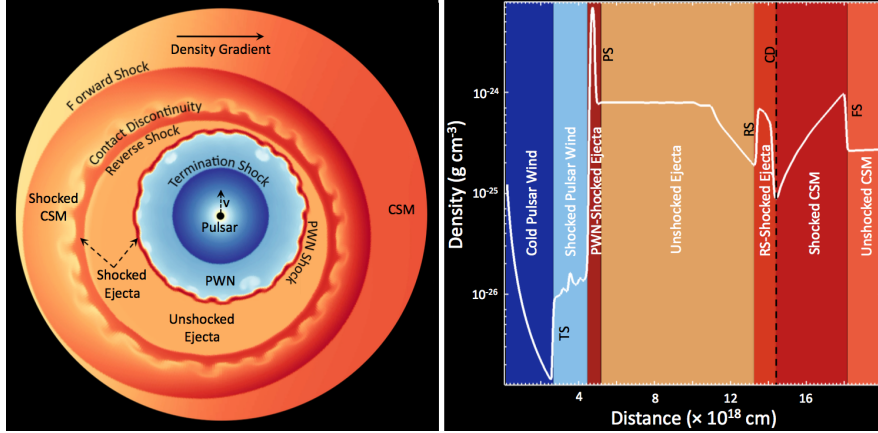
Fig. 3 Left: Density image from a hydrodynamical simulation of a PWN expanding into an SNR that is evolving into a medium with a CSM density gradient increasing to the right. The pulsar itself is moving upward. The reverse shock is propagating inward, approaching the PWN preferentially from the upper right due to the combined effects of the pulsar motion and the CSM density gradient. Right: Density profile for a radial slice through the simulated composite SNR. Colored regions correpond to different physical regions identified in the SNR image.

wave expands freely at a speed of $\sim (5-10) \times 10^3$ km s^{-1}, much higher than typical pulsar velocities of $\sim 200 - 1500$ km s^{-1}. As a result, for young systems the pulsar will always be located near the SNR center.

The energetic pulsar wind is injected into the SNR interior, forming a high-pressure bubble that expands supersonically into the surrounding ejecta, forming a shock. The input luminosity is generally assumed to have the form (e.g. Pacini & Salvati 1973)

$$\dot{E} = \dot{E}_0 \left(1 + \frac{t}{\tau_0} \right)^{-\frac{(n+1)}{(n-1)}} \tag{13}$$

where

$$\tau_0 \equiv \frac{P_0}{(n-1)\dot{P}_0} \tag{14}$$

is the initial spin-down time scale of the pulsar. Here $\dot{E}_0$ is the initial spin-down power, P_0 and $\dot{P}_0$ are the initial spin period and its time derivative, and n is the so-called "braking index" of the pulsar ($n = 3$ for magnetic dipole spin-down). The pulsar has roughly constant energy output until a time τ_0, beyond which the output declines fairly rapidly with time.

Figure 3 illustrates the evolution of a PWN within its host SNR. The left panel shows a hydrodynamical simulation of an SNR evolving into a non-uniform medium, with a density gradient increasing from left to right. The pulsar is moving upward. The SNR forward shock (FS), RS and contact discontinuity (CD) separating the shocked CSM and shocked ejecta are identified, as is the PWN shock driven

by expansion into the cold ejecta. The right panel illustrates the radial density distribution, highlighting the PWN TS as well as the SNR FS, CD, and RS.

4.1 Early Expansion

The energetic pulsar wind injected into the SNR interior forms a high-pressure bubble that drives a shock into the surrounding ejecta. The sound speed in the relativistic fluid within the PWN is sufficiently high ($c_s = c/\sqrt{3}$) that any pressure variations experienced during the expansion are quickly balanced within the bubble; at early stages, the pulsar thus remains located at the center of the PWN, even if the pulsar itself is moving through the inner SNR, which is often the case because pulsars can be born with high velocities ($\sim 200 - 1500$ km s^{-1}; Arzoumanian et al. 2002) due to kicks imparted in the supernova explosions. The wind is confined by the innermost slow-moving ejecta, and the PWN expansion drives a shock into these ejecta, heating them and producing thermal emission. Magnetic tension in the equatorial regions exceeds that elsewhere in the nebula, resulting an a oblate morphology with the long axis aligned with the pulsar rotation axis (Begelman & Li 1992). As illustrated in Figure 3 (left), the PWN/ejecta interface is susceptible to Rayleigh-Taylor (R-T) instabilities. These structures are readily observed in the Crab Nebula (Figure 1a; also see Hester 2008 as well as Chapter "Supernova of 1054 and its remnant, the Crab Nebula"), where highly-structured filaments of gas and dust are observed in the optical and infrared. Spectral studies of these filaments provide information on the composition, mass, and velocity of the ejecta. This, along with information about the associated SNR, can place strong constraints on the progenitor system.

In the Crab Nebula, for example, the total mass of the ejecta swept up by the PWN is $\sim 5 M_\odot$ (Fesen et al. 1997), and the expansion velocity is ~ 1300 km s^{-1} (Temim et al. 2006). The Crab is one of a small set of young PWNe for which there is no evidence of the surrounding SNR, other than the swept-up ejecta. Other examples include 3C 58 and perhaps G54.1+0.3, although there is some evidence for radio and X-ray emission that might be associated with an SNR shell in the latter (Bocchino et al. 2010). The lack of bright (or any) SNR emission in these systems is generally assumed to result from some combination of low explosion energy, as might result from low-mass progenitors that produce electron-capture SNe, and a very low surrounding density, as could result from mass loss through stellar winds in the late phase of massive star evolution.

For the Crab Nebula, the available evidence appears to be consistent with a low-mass progenitor (Yang & Chevalier 2015). For G54.1+0.3, on the other hand, an infrared shell surrounding the X-ray PWN is observed to encompass a collection of what appear to be O-type stars that presumably formed in the same stellar cluster as the PWN progenitor, indicating that this system resulted from a high mass star (Temim et al. 2010). The IR emission appears to arise from a combination of slow shocks driven into the surrounding ejecta and unshocked supernova dust that is being radiatively heated by emission from the embedded stars.
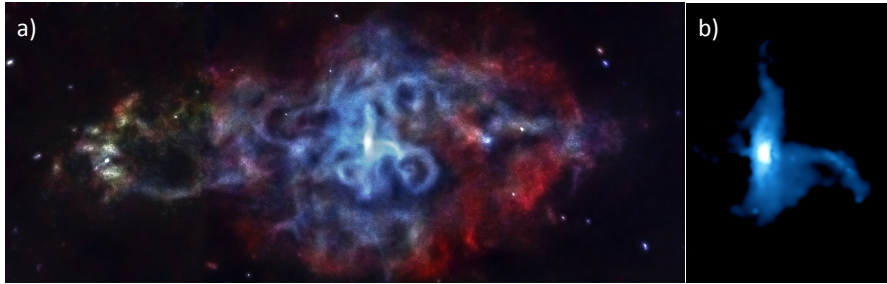
Fig. 4 a) *Chandra* image of 3C 58 (Slane et al. 2004). Low (high) energy X-rays are shown in red (blue). b) Expanded view of the central region of 3C 58 showing the toroidal structure and jet associated with the central pulsar. [Images courtesy NASA/CXO.]

While the optical emission from 3C 58 shows evidence for R-T structures, high resolution X-ray observations show a network of filamentary structures that do not appear to be associated with the optical filaments (Figure 4). The origin of these structures is currently not understood, although kink instabilities in the termination shock region may result in magnetic structures whose size scale is similar to what is observed in 3C 58 (Slane et al. 2004). Thermal X-ray emission is observed in the outer regions of the PWN, (which appear red in Figure 4 due to both the low energy thermal flux and the steepening of the synchrotron spectrum with radius associated with burn-off of high energy particles) with indications of enhanced metals as would be expected from shocked ejecta. Mass and abundance measurements, combined with expansion measurements, can provide the velocity and composition distribution of the ejecta, placing constraints on the total ejecta mass and explosion energy of the supernova (e.g., Yang & Chevalier 2015, Gelfand et al. 2015).

For more typical systems, the ambient density (and/or supernova explosion energy) is sufficiently high to form a distinct SNR shell of swept-up CSM/ISM material, accompanied by RS-shocked ejecta, as illustrated in Figure 3. An exceptional example is G21.5−0.9. X-ray observations (Figure 5a) show a bright central nebula that coincides with a flat-spectrum radio nebula. The nebula is accompanied by a faint SNR shell (Slane et al. 2000; Matheson & Safi-Harb 2005), and radio timing measurements with the Parkes telescope reveal the 62 ms pulsar J1833-1034 in the center of the nebula (Camilo et al. 2006). Ground-based IR observations (Zajczyk et al. 2012) reveal a ring of [Fe II] emission associated with ejecta that has been swept up by the expanding PWN (Fig. 4b; contours are X-ray emission from the dashed square region from Fig. 4a). The emission directly around the pulsar is extended in X-rays (see innermost contours), possibly associated with a surrounding torus as is seen in the Crab Nebula and other PWNe. The IR emission surrounding the pulsar is polarized. The electric field vectors are shown in Fig. 4c, with the length of the white bars proportional to the polarization fraction. The magnetic field, which is perpendicular to the electric vectors, is largely toroidal, consistent with the picture of wound-up magnetic flux from the spinning pulsar, as described above.
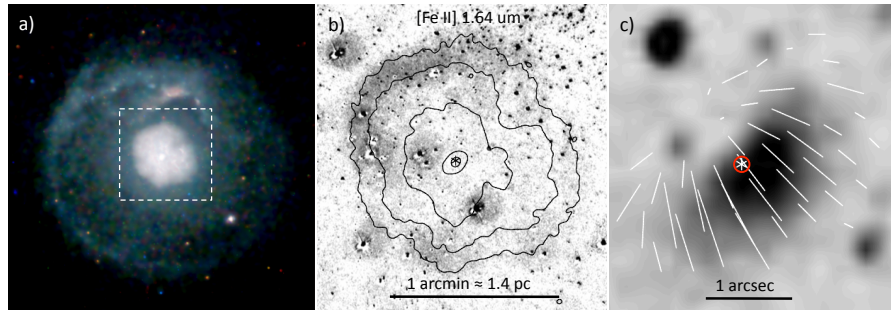
Fig. 5 a) *Chandra* image of G21.5−−.9. The pulsar is located at the center and is surrounded by a PWN. The faint outer shell is the SNR, and a portion of the emission between the PWN and the outer shell is scattered flux from the PWN. b) Infrared image at 1.64 μm showing a shell of [Fe II] emission from ejecta that has been swept up and shocked by the expanding PWN. c) Infrared polarization image. The pulsar is within the red circle. White bars show the direction of the electric field vectors, with the length proportional to the polarization fraction. The inferred magentic field, which is orthogonal to the electric vectors, is largely toroidal. [From Zajczyk et al. 2012, A&A, 542, A12 - Reproduced with permission from Astronomy & Astrophysics, ©ESO]

4.2 Reverse-shock Interaction

As the SNR blast wave sweeps up increasing amounts of material, the RS propagates back toward the SNR center. In the absence of a central PWN, it reaches the center at a time $t_c \approx 7(M_{ej}/10\,M_\odot)^{5/6}E_{51}^{-1/2}n_0^{-1/3}$ kyr, where E_{51} is the explosion energy, M_{ej} is the ejecta mass, and n_0 is the number density of ambient gas (Reynolds & Chevalier 1984). When a PWN is present, however, the RS interacts with the the nebula before it can reach the center (Figure 3). The shock compresses the PWN, increasing the magnetic field strength and resulting in enhanced synchrotron radiation that burns off the highest energy particles. In the simplified case of SNR expansion into a uniform medium, with a spherically-symmetric PWN, the system evolves approximately as illustrated in Figure 2 (from Gelfand et al. 2009), where the Sedov solution has been assumed for the SNR evolution,

$$R_{SNR} \approx 6.2 \times 10^4 \left(\frac{E_{SN}}{n_0} \right)^{1/5} t^{2/5}, \tag{15}$$

and the PWN evolves approximately as

$$R_{PWN} \approx 1.5\dot{E}_0^{1/5}E_{SN}^{3/10}M_{ej}^{-1/2}t^{6/5} \tag{16}$$

(Chevalier 1977) prior to the RS interaction. [In reality, the SNR expands freely at the outset, approaching the Sedov solution as $t \to t_c$.] Here, E_{SN} is the supernova explosion energy, n_0 is the number density of the ambient medium, and M_{ej} is the mass of the supernova ejecta.
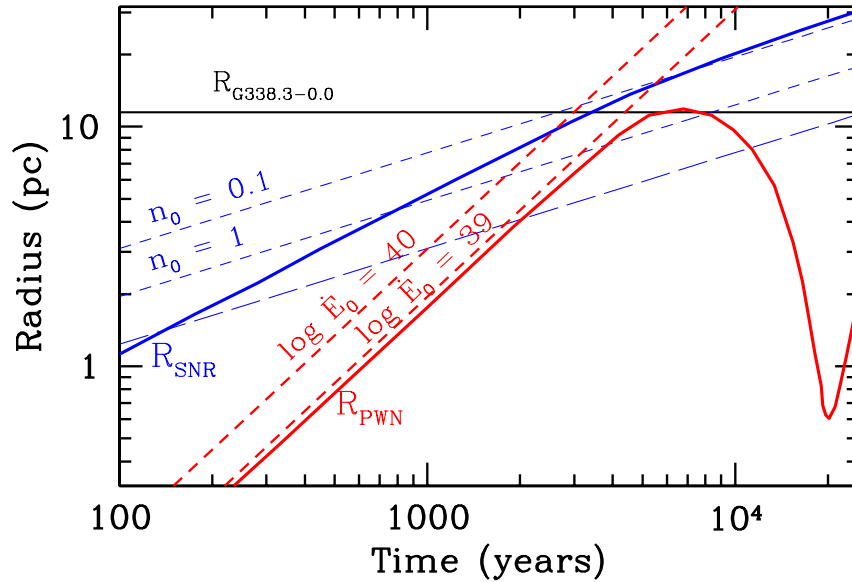
Fig. 6 Time evolution of the SNR and PWN radii for a range of values for the ambient density and initial spin-down power of the pulsar. The solid curves correspond to models from Gelfand et al. (2009) using $\dot{E}_0 = 10^{40}$ erg s^{-1}, $M_{ej} = 8M_\odot$, $n_0 = 0.1$ cm^{-3}, and $E_{51} = 1$.

If the ambient CSM/ISM is significantly nonuniform (and it typically is, because massive stars form in turbulent regions of dense clouds, and strongly modify the CSM through strong and potentially-asymmetric winds), the FS expands more (less) rapidly in regions of lower (higher) density. This has two significant effects. First, it changes the morphology of the SNR to a distorted shell for which the associated pulsar is no longer at the center. Second, the RS also propagates asymmetrically, reaching the center more quickly from the direction of the higher density medium (Blondin et al. 2001).

The return of the RS ultimately creates a collision with the PWN. During the compression phase, the magnetic field of the nebula increases, resulting in enhanced synchrotron radiation and significant radiative losses from the highest energy particles. The PWN/RS interface is Rayleigh-Taylor (R-T) unstable, and is subject to the formation of filamentary structure where the dense ejecta material is mixed into the relativistic fluid. If the SNR has evolved in a nonuniform medium, an asymmetric RS will form, disrupting the PWN and displacing it in the direction of lower density (Figure 3). The nebula subsequently re-forms as the pulsar injects fresh particles into its surroundings, but a significant relic nebula of mixed ejecta and relativistic gas will persist.

Because the SNR RS typically reaches the central PWN on a timescale that is relatively short compared with the SNR lifetime, all but the youngest PWNe that we observe have undergone an RS interaction (see Figure 6). This has significant

impact on the large-scale geometry of the PWN, as well as on its spectrum and dynamical evolution. Remnants such as G328.4+0.2 (Gelfand et al. 2007), MSH 15−56 (Temim et al. 2013), and G327.1−1.1 (Temim et al. 2015) all show complex structure indicative of RS/PWN interactions, and observations of extended sources of very high energy (VHE) γ-rays indicate that many of these objects correspond to PWNe that have evolved beyond the RS-crushing stage.

An example of such a RS-interaction stage is presented in Figure 7 where we show the composite SNR G327.1−1.1 (Temim et al. 2015). Radio observations (a) show a complete SNR shell surrounding an extended flat-spectrum PWN in the remnant interior, accompanied by a finger-like structure extending to the northwest. X-ray observations (b) show faint emission from the SNR shell along with a central compact source located at the tip of the radio finger, accompanied by a tail of emission extending back into the radio PWN. The X-ray properties of the compact source are consistent with emission from a pulsar (though, to date, pulsations have not yet been detected) which, based on its position relative to the geometric center of the SNR, appears to have a northward motion. Spectra from the SNR shell indicate a density gradient in the surrounding medium, increasing from east to west. Results from hydrodynamical modeling of the evolution of such a system using these measurements as constraints, along with an estimate for the spin-down power of the pulsar based upon the observed X-ray emission of its PWN (see Section 3.1) are shown in Figure 7c where we show the density (compare with Figure 3). The RS has approached rapidly from the west, sweeping past the pulsar and disrupting the PWN. The result is a trail of emission swept back into the relic PWN, in excellent agreement with the radio morphology. The X-ray spectrum of the tail shows a distinct steepening with distance from the pulsar, consistent with synchrotron cooling of the electrons based on the estimated magnetic field and age of the injected particles tracked in the hydro simulation. Detailed investigation shows that the central source is actually resolved, suggesting that the pulsar is surrounded by a compact nebula (panel d). This is embedded in a cometary structure produced by a combination of the northward motion of the pulsar and the interaction with the RS propagating from the west. However, extended prong-like structures are observed in X-rays, whose origin is currently not understood.

4.3 Late-phase Evolution

As illustrated in Figure 2, as a PWN ages, the ratio of the IC to synchrotron luminosity increases due to the declining magnetic field in the nebula. As a result, in late phases of the evolution, the γ-ray emission may dominate that observed in the radio or X-ray bands. Indeed, PWNe dominate the population of TeV γ-ray sources in the Galactic Plane (e.g., Carrigan et al. 2013). For many such TeV-detected PWNe, the inferred magnetic field strengths are only $\sim 5\ \mu$G (e.g., de Jager et al. 2008). In such a case, 1 TeV gamma-rays originate from electrons with energies of ~ 20 TeV (assuming IC scattering of CMB photons) while 1 keV synchrotron X-rays originate
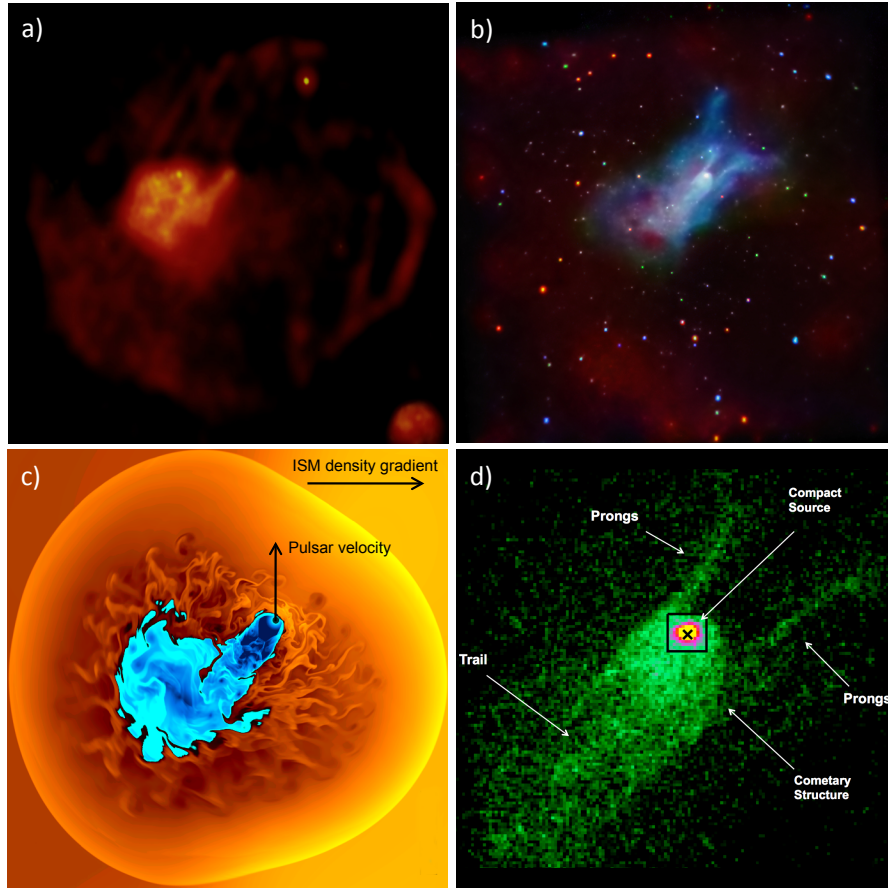
Fig. 7 a) Radio emission from G327.1−1.1 (SIFA/MOST, CSIRO/ATNF/ATCA) showing SNR shell surrounding central PWN. b) *Chandra* image showing faint X-ray SNR shell and PWN. c) Hydrodynamical simulation of evolved composite SNR with properties similar to G327.1−1.1. (See text for details.) d) Expanded *Chandra* view of central region of G327.1−1.1. A compact nebula surrounding the neutron star is embedded in a cometary structure with an extended tail, formed by a combinition of northward pulsar motion and an interaction with the SNR reverse shock approaching from the west. Prong-like structures of unknown origin extend from several regions around the nebula. [After Temim et al. 2015. All images have north at top and west at the right.]

from electrons with energies of ∼ 100 TeV (see Eqns. 9, 12). The higher energy X-ray producing electrons fall beyond the cooling break, while those producing the γ-rays are predominantly uncooled. The result is a bright TeV nebula accompanied by a fainter X-ray nebula.

Such results are seen clearly for HESS J1825−137, for which measurements show that the TeV emission extends to much larger distances than the X-ray emission due to more rapid cooling of the X-ray emitting particles. Indeed, for this PWN,
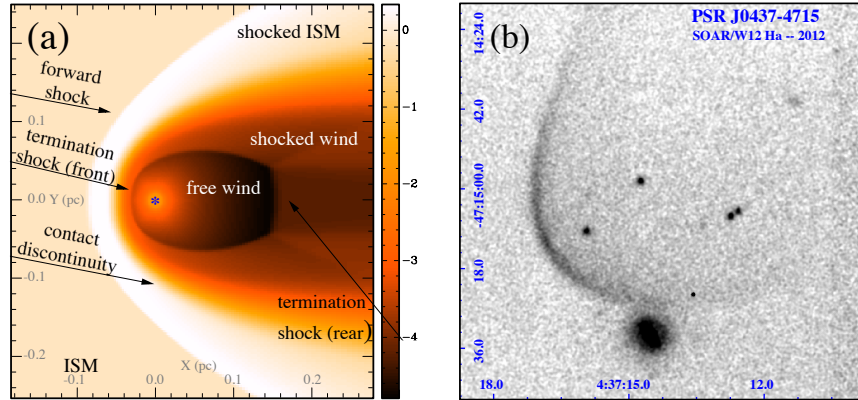
Fig. 8 Left: Hydrodynamic simulation of a pulsar bow shock nebula (see text). [From Gaensler & Slane 2006. Reprinted by permission.] Right: Hα image of bow shock created by PSR J0437−4715. [Image courtesy of R. Romani. See Brownsberger & Romani 2014.]

the γ-ray size is observed to decline with increasing energy, indicating that even some of the γ-ray emitting electrons fall beyond the cooling break although, as observed in younger PWNe in X-rays, the high energy emission extends to larger radii than can be explained unless rapid diffusion of the associated electrons is occurring (Van Etten & Romani 2011). Deep surveys with future VHE γ-ray telescopes are expected to reveal many older systems for which emission in other wavebands is now faint.

4.4 Escaping the SNR – Bow Shock PWNe

Late in the evolution of a PWN, the pulsar will exit its host SNR and begin traveling through the ISM. Since the sound speed for the cold, warm, and hot phases of the ISM is $v_s \sim 1$, 10, and 100 km s^{-1}, the pulsar motion will be supersonic. The relative motion of the ISM sweeps the pulsar wind back into a bow shock structure. As illustrated in Figure 8 (left), the structure is still characterized by an FS, CD, and TS, but the gas behind the FS is now shocked ISM material, and the CD separates the shocked pulsar wind from the shocked ISM. Inside the TS, the pulsar wind flows freely. The distance from the pulsar to the TS depends on the angle θ relative to the pulsar motion (as does that to the FS), and is approximately described by (Wilkin 1996)

$$R_w(\theta) = R_{w0} \frac{\sqrt{3(1 - \theta \cot \theta)}}{\sin \theta}. \tag{17}$$

Here R_{w0} is the stand-off distance from the pulsar, in the direction of motion, where the wind pressure matches the ram pressure of the inflowing ISM (in the pulsar frame):

$$R_{w0} = \sqrt{\dot{E}/(r\pi\omega c\rho_0 v_{\mathrm{PSR}}^2)},\tag{18}$$

where v_{PSR} is the pulsar velocity and ρ_0 is the density of the unshocked ISM (cf. Equation 6). Although this description was derived for a non-relativistic, unmagnetized radiative fluid, while the pulsar wind is magnetized and relativistic, and the radiative time for the ISM is long relative to the flow timescale in pulsar bow shock nebulae, the overall geometric description provides an adequate representation (Bucciantini & Bandiera 2001).

The non-radiative shock formed in the ISM interaction results in the emission of optical Balmer lines, dominated by Hα, providing a distinct signature from which properties of the pulsar motion and wind luminosity can be inferred. An exceptional example is the bow shock nebula associated with PSR J0437$-$4715 (Figure 8, right), a nearby ms pulsar in a binary system, for which timing measurements have established $M_{NS} \sim 1.8 M_{\odot}$ (Verbiest et al. 2008). Parallax measurements establish a distance of 0.16 kpc, and proper motion measurements of the pulsar (and nebula) provide $v_{\perp} = 107$ km s^{-1}. With the measured spin-down power $\dot{E} = 5.5 \times 10^{33}$ erg s^{-1}, modeling of the bow shock structure provides a direct limit on the NS moment of inertia that indicates a relatively stiff equation of state (Brownsberger & Romani 2014).

Radio and X-ray measurements of bow shock nebulae probe the shocked pulsar wind. Observations of PSR J1747$-$2958 and its associated nebula G359.23$-$0.82 reveal a long radio tail and an X-ray morphology that reveals both a highly magnetized tail from wind shocked from the forward direction, and a weakly magnetized tail from wind flowing in the direction opposite that of the pulsar motion (Gaensler et al. 2004). High resolution measurements of the emission near several pulsars have also provided evidence for asymmetric pulsar winds imprinting additional structure on the bow shock structure (e.g., Romani et al. 2010).

5 Summary

The structure of a PWN is determined by both the properties of the host pulsar and the environment into which the nebula expands. Observations across the electromagnetic spectrum allow us to constrain the nature of the pulsar wind, including both its magnetization and geometry, and the global properties of the PWN allow us to constrain the evolutionary history as it evolves through the ejecta of the supernova remnant in which it was born. Spectroscopic observations yield information on the mass and composition of shocked ejecta into which the nebula expands, and on the expansion velocity. Measurements of the broadband spectrum provide determinations of the nebular magnetic field and the maximum energy of the particles injected into the PWN. These observations continue to inform theoretical models of relativistic shocks which, in turn, have broad importance across the realm of high-energy astrophysics.

At late phases, interactions between the PWN and the SNR RS produce a complex combination of the relic nebula and freshly-injected particles. Hydrodynamical simulations of the entire composite SNR system can reveal information on the long-term evolution, which depends on the details of the pulsar motion, its wind properties, the ejecta mass and explosion energy of the SNR, and the properties of the surrounding medium. Such systems may eventually fade into obscurity, with γ-ray emission from the relic electrons providing an important signature before the pulsars exit their SNRs and traverse the ISM at supersonic speeds, producing elongated bow shock nebulae whose structure continue to provide a glimpse of the relativistic outflows from the aging pulsars.

Acknowledgements

Cross-References

- Supernova of 1054 and its remnant, the Crab Nebula
- The Historical Supernova of AD1181 and its remnant, 3C58
- Supernovae from super AGB Stars (8-12 $M_\odot$)
- Explosion Physics of Core - Collapse Supernovae
- Radio Neutron Stars
- Distribution of the spin periods of neutron stars
- Dynamical Evolution and Radiative Processes of Supernova Remnants
- X-ray Emission Properties of supernova remnants
- Infrared Emission from Supernova Remnants: Formation and Destruction of Dust

References

1. Arzoumanian Z, Chernoff DF., Cordes JM (2002) The Velocity Distribution of Isolated Radio Pulsars. ApJ 568:289-301
2. Atoyan AM, Aharonian FA (1996) On the mechanisms of gamma radiation in the Crab Nebula. MNRAS 278:525-541
3. Begelman MC, Li Z-Y (1992) An axisymmetric magnetohydrodynamic model for the Crab pulsar wind bubble. ApJ 397:187-195
4. Blondin JM, Chevalier RA, Frierson DM (2001) Pulsar Wind Nebulae in Evolved Supernova Remnants. ApJ 563:806
5. Bocchino F, Bandiera R., Gelfand JD (2010) XMM-Newton and SUZAKU detection of an X-ray emitting shell around the pulsar wind nebula G54.1+0.3. A&A 520A:71
6. Bogovalov SV (1999) On the physics of cold MHD winds from oblique rotators. A&A 349:1017
7. Brownsberger S, Romani RW (2014) A Survey for H-alpha Pulsar Bow Shocks, ApJ 784:154
8. Bucciantini N (2011) MHD models of Pulsar Wind Nebulae. ASSP 21:473
9. Bucciantini N, Bandiera R (2001) Pulsar bow-shock nebulae. I. Physical regimes and detectability conditions. A&A 375:1032-1039

10. Camilo F, Ransom SM, Gaensler BM, Slane P, Lorimer DR, Reynolds J, et al. (2006) PSR J1833-1034: Discovery of the Central Young Pulsar in the Supernova Remnant G21.5-0.9. ApJ 637:456-465

11. Carrigan F, Brun F, Chaves RCG, Deil C, Donath A, Gast H, et al. (2013) The H.E.S.S. Galactic Plane Survey - maps, source catalog and source population. In: Proceedings of the 33rd International Cosmic Ray Conference (arXiv:1307.4690)

12. Chevalier RC (1977) Was SN 1054 A Type II Supernova? In: Schramm DN (ed) Supernovae, Astrophysics and Space Science Library 66:53

13. de Jager OC, Slane PO, LaMassa S (2008) Probing the Radio to X-Ray Connection of the Vela X Pulsar Wind Nebula with Fermi LAT and H.E.S.S. ApJ 689:L125

14. Fesen RA, Shull JM, Hurford AP (1997) An Optical Study of the Circumstellar Environment Around the Crab Nebula. AJ 113:354-363

15. Gaensler BM, van der Swaluw E, Camilo F, Kaspi VM, Baganoff FK, Yusef-Zadeh F, et al. (2004) The Mouse that Soared: High-Resolution X-Ray Imaging of the Pulsar-powered Bow Shock G359.23-0.82. ApJ 616:383-402

16. Gaensler BM, Slane PO (2006) The Evolution and Structure of Pulsar Wind Nebulae. ARA&A 44:17-47

17. Gelfand JD, Gaensler BM, Slane PO, Patnaude DJ, Hughes JP, Camilo, F (2007) The Radio Emission, X-Ray Emission, and Hydrodynamics of G328.4+0.2: A Comprehensive Analysis of a Luminous Pulsar Wind Nebula, Its Neutron Star, and the Progenitor Supernova Explosion. ApJ 663:468-486

18. Gelfand, JD, Slane, PO, Zhang, W (2009) A Dynamical Model for the Evolution of a Pulsar Wind Nebula Inside a Nonradiative Supernova Remnant. ApJ 703:2051-2067

19. Gelfand JD, Slane PO, Temim T. (2015) The Properties of the Progenitor Supernova, Pulsar Wind, and Neutron Star inside PWN G54.1+0.3. ApJ 807:30

20. Goldreich P, Julian WH (1969) Pulsar Electrodynamics. ApJ 157:869

21. Hester JJ (2008) The Crab Nebula: An Astrophysical Chimera. ARA&A 46:127-155

22. Kargaltsev O, Cerutti B, Lyubarsky Y, Striani E (2015) Pulsar-Wind Nebulae. Recent Progress in Observations and Theory. SSRv 191:391-439

23. Kennel CF, Coroniti FV (1984) Magnetohydrodynamic model of Crab nebula radiation. ApJ 283:710-730

24. Lyubarsky YE (2002) On the structure of the inner Crab Nebula. MNRAS 329:L34-L36

25. Lyubarsky YE (2003) The termination shock in a striped pulsar wind. MNRAS 345:153

26. Matheson H, Safi-Harb S (2005) The plerionic supernova remnant G21.5-0.9: In and out. AdSpR 35:1099-1105

27. Pacini F, Salvati M (1973) On the Evolution of Supernova Remnants. Evolution of the Magnetic Field, Particles, Content, and Luminosity. ApJ 186:249-266

28. Possenti A, Cerutti R, Colpi M, Mereghetti S (2002) Re-examining the X-ray versus spin-down luminosity correlation of rotation powered pulsars. A&A 387:993-1002

29. Reynolds, SP, Chevalier, RA (1984) Evolution of pulsar-driven supernova remnants. ApJ 278:630-648

30. Romani RW, Shaw MS, Camilo F, Cotter G, Sivakoff GR (2010) The Balmer-dominated Bow Shock and Wind Nebula Structure of gamma-ray Pulsar PSR J1741-2054. ApJ 724:908-914

31. Sironi L, Spitkovsky A (2011) Acceleration of Particles at the Termination Shock of a Relativistic Striped Wind. ApJ 741:39

32. Sironi L, Spitkovsky A, Arons J (2013) The Maximum Energy of Accelerated Particles in Relativistic Collisionless Shocks. ApJ 771:54

33. Slane P, Chen Y, Schulz NS, Seward FD, Hughes JP, Gaensler BM (2000) Chandra Observations of the Crab-like Supernova Remnant G21.5-0.9 ApJ 533:L29-L32

34. Slane P, Helfand DJ, van der Swaluw E, Murray SS (2004) New Constraints on the Structure and Evolution of the Pulsar Wind Nebula 3C 58. ApJ 616:403-413

35. Slane P, Helfand DJ, Reynolds SP, Gaensler BM, Lemiere A, Wang Z (2008) The Infrared Detection of the Pulsar Wind Nebula in the Galactic Supernova Remnant 3C 58. ApJ 676:L33

36. Tang X, Chevalier RA (2012) Particle Transport in Young Pulsar Wind Nebulae ApJ 752:83

37. Temim T, Gehrz RD, Woodward CE, Roellig TL, Smith, N, Rudnick, L, et al. (2006) Spitzer Space Telescope Infrared Imaging and Spectroscopy of the Crab Nebula. AJ 132:1610-1623
38. Temim T, Slane P, Reynolds SP, Raymond JC, Borkowski, KJ (2010) Deep Chandra Observations of the Crab-like Pulsar Wind Nebula G54.1+0.3 and Spitzer Spectroscopy of the Associated Infrared Shell. ApJ 710:309-324
39. Temim T, Slane P, Castro D, Plucinsky PP, Gelfand J, Dickel JR (2013) High-energy Emission from the Composite Supernova Remnant MSH 15-56. ApJ 768:61
40. Temim T, Slane P, Kolb C, Blondin J, Hughes JP, Bucciantini N (2015) Late-Time Evolution of Composite Supernova Remnants: Deep Chandra Observations and Hydrodynamical Modeling of a Crushed Pulsar Wind Nebula in SNR G327.1-1.1. ApJ 799:158
41. Timokhin AN, Harding AK (2015) On the Polar Cap Cascade Pair Multiplicity of Young Pulsars. ApJ 810:144
42. Torres D, Martn J, de Oa Wilhelmi E, Cillis A (2013) The effects of magnetic field, age and intrinsic luminosity on Crab-like pulsar wind nebulae. MNRAS 436:3112-3127
43. van der Swaluw E (2003) Interaction of a magnetized pulsar wind with its surroundings. MHD simulations of pulsar wind nebulae. A&A 404:939-947
44. Van Etten A, Romani RW (2011) Multi-zone Modeling of the Pulsar Wind Nebula HESS J1825-137. ApJ 742:62
45. Verbiest JPW, Bailes M, van Straten W, Hobbs, GB, Edwards RT, Manchester RN et al. (2008) Precision Timing of PSR J0437-4715: An Accurate Pulsar Distance, a High Pulsar Mass, and a Limit on the Variation of Newton's Gravitational Constant. ApJ 679:675-680
46. Wilkin FP (1996) Exact Analytic Solutions for Stellar Wind Bow Shocks. ApJ 459:L31
47. Yang H, Chevalier RC (2015) Evolution of the Crab Nebula in a Low Energy Supernova ApJ 806:153
48. Zajczyk A, Gallant YA, Slane P, Reynolds SP, Bandiera R, Gouiffs C (2012) Infrared imaging and polarimetric observations of the pulsar wind nebula in SNR G21.5-0.9. A&A 542:A12